PHOTONICS Research

Perfect light absorber with a PT phase transition via coupled topological interface states

Jiajun Zheng,[1] Haiyang Zhou,[2] Junyang Li,[2] Yufei Wang,[3,5] Haitao Jiang,[1,6] Yunhui Li,[1,4] Zhiwei Guo,[1] Yaping Yang,[1] Guiqiang Du,[2,7] Wanhua Zheng,[3] Yong Sun,[1,8] and Hong Chen[1]

[1]MOE Key Laboratory of Advanced Micro-structured Materials, School of Physics Sciences and Engineering, Tongji University, Shanghai 200092, China
[2]School of Space Science and Physics, Shandong University, Weihai 264209, China
[3]State Key Laboratory on Integrated Optoelectronics, Institute of Semiconductors, Chinese Academy of Sciences, Beijing 100083, China
[4]Department of Electrical Engineering, Tongji University, Shanghai 201804, China
[5]e-mail: yufeiwang@semi.ac.cn
[6]e-mail: jiang-haitao@tongji.edu.cn
[7]e-mail: dgqql@sdu.edu.cn
[8]e-mail: yongsun@tongji.edu.cn

Received 16 November 2022; revised 5 January 2023; accepted 14 January 2023; posted 18 January 2023 (Doc. ID 480697); published 9 March 2023

Recently, the concepts of parity–time (PT) symmetry and band topology have inspired many novel ideas for light manipulation in their respective directions. Here we propose and demonstrate a perfect light absorber with a PT phase transition via coupled topological interface states (TISs), which combines the two concepts in a one-dimensional photonic crystal heterostructure. By fine tuning the coupling between TISs, the PT phase transition is revealed by the evolution of absorption spectra in both ideal and non-ideal PT symmetry cases. Especially, in the ideal case, a perfect light absorber at an exceptional point with unidirectional invisibility is numerically obtained. In the non-ideal case, a perfect light absorber in a broken phase is experimentally realized, which verifies the possibility of tailoring non-Hermiticity by engineering the coupling. Our work paves the way for novel effects and functional devices from the exceptional point of coupled TISs, such as a unidirectional light absorber and exceptional-point sensor.

https://doi.org/10.1364/PRJ.480697

1. INTRODUCTION

Topological interface states (TISs) in photonic heterostructures composed of two 1D photonic crystals (PCs) with different bulk band topologies have attracted researchers' considerable interest [1–6]. It has been shown that a quantized number called the Zak phase assigned to every band can be defined for PCs with inversion symmetry, and the Zak phases between two bands can be exchanged with a topological transition [7,8]. It is worth mentioning that the topological transition in PCs can also be revealed with the transition between two effective single negative media [9,10] in the bandgap. In practice, different band topologies can be related to the sign of the reflection phase for the gap [11–14]. TIS can greatly enhance light–matter interaction including enhancement of nonreciprocal radiation [15,16], as its smaller mode volume leads to an increased Purcell factor [17]. For instance, strongly coupled TISs have been theoretically investigated to achieve multi-band perfect absorption [18,19] and strong Rabi splitting [20]. Very recently, TISs have been used to explore high-order topological properties with synthetic dimensions [21].

On the other hand, since Bender *et al.* [22] proposed a class of non-Hermitian Hamiltonians whose real spectra can be ensured by parity–time (PT) symmetry [23], PT-symmetric systems have been widely investigated in photonics [24], acoustics [25], circuits [26], and atom physics [27]. After the early observations of PT phase transitions in the field of optics [28,29], a variety of intriguing phenomena in optical PT-symmetric systems were exploited, including loss-induced revival of lasing [30], unidirectional propagation [31] and invisibility [32,33], negative refraction [34], coherent perfect absorption (CPA) [35,36], etc. The phase transition takes place at the so-called "exceptional point" (EP) [37], where not only eigenvalues merge with each other, but also their corresponding eigenvectors become completely parallel.

In recent years, many novel applications of PT-symmetric photonic structures have been proposed [38,39], such as a single mode laser [40,41] and a integrated orbital angular momentum microlaser [42]. Particularly, the advantages of the non-Hermitian degeneration (coalescence of both eigenvalues and eigenstates) at EP in detecting and sensing have attracted much

attention [43–45], including single nanoparticle detection [46], microelectromechanical systems (MEMS)-based implantable wireless sensing [47,48], and weak nonlinearity sensing [49]. Very recently, based on an optical system of coupled whispering gallery mode microcavities, optical CPA at EP has been demonstrated [50].

The combination of topology and non-Hermitian physics leads to many novel phenomena, including the non-Hermitian skin effect [51], recovery of topological zero mode [52], interplay with nonlinearity [53], etc. Recently, a flip-of-state phenomenon related to the topology of EP in a non-Hermitian system has been widely discussed [54,55]. Researchers have also investigated EP in topological systems such as a Kitaev chain [56] and quasiperiodic Aubry–Andre–Harper model [57]. Novel sensors [58] and new concepts of topological wireless power transfer [59,60] involving coupled topological states [61] have been proposed based on these findings. Given that topological states can greatly enhance light–matter interactions, the introduction of TISs into a PT-symmetric system working around EP is a straightforward approach to improve the performance of non-Hermitian photonic structures.

Nevertheless, there is a lack of experimental demonstration of perfect absorption at EP in topological photonic systems where the coupling strength between TISs is comparable to the dissipation.

In this paper, we propose and investigate a perfect light absorber (so called one-channel CPA [62]) with two coupled TISs. We calculate spectral responses for these TISs using coupled mode theory (CMT), which are consistent with numerical simulations obtained from the transfer matrix method (TMM). By carefully adjusting the scattering losses of TISs, a passive but ideal PT-symmetric system is achieved from the perspective of an effective Hamiltonian [36,63]. With a decrease in coupling between two TISs, the two perfect absorption peaks are preserved at the beginning but gradually get close to each other, until they merge at EP. After that, the absorption peak begins to decline. These featured spectral responses reveal the PT phase transition near EP. Also, unidirectional invisibility at EP is numerically obtained. Results in the non-ideal case are similar, except that the absorption peaks of coupled TISs in the PT-symmetric phase are not perfect, and the maximum value of absorption in the broken phase changes non-monotonically as coupling decreases. In particular, perfect light absorption can be observed with critical coupling in the PT-broken phase. We experimentally demonstrate such a perfect light absorber in the non-ideal case, which verifies the possibility of tailoring non-Hermiticity by engineering the coupling. Our work paves the way for novel effects and functional devices from EP of coupled TISs, such as a unidirectional light absorber and EP sensor.

2. EFFECTIVE HAMILTONIAN WITH PT SYMMETRY IN COUPLED TISS

The proposed PC structure with coupled TISs under normal incidence is shown in Fig. 1(a), which comprises $(ABA)_v$, $(DCD)_u$, and a silver layer M. Layers A and C are titanium dioxide with a refractive index of $n_1 = 2.12$, B and D are silicon dioxide with a refractive index of $n_2 = 1.43$, and v and u

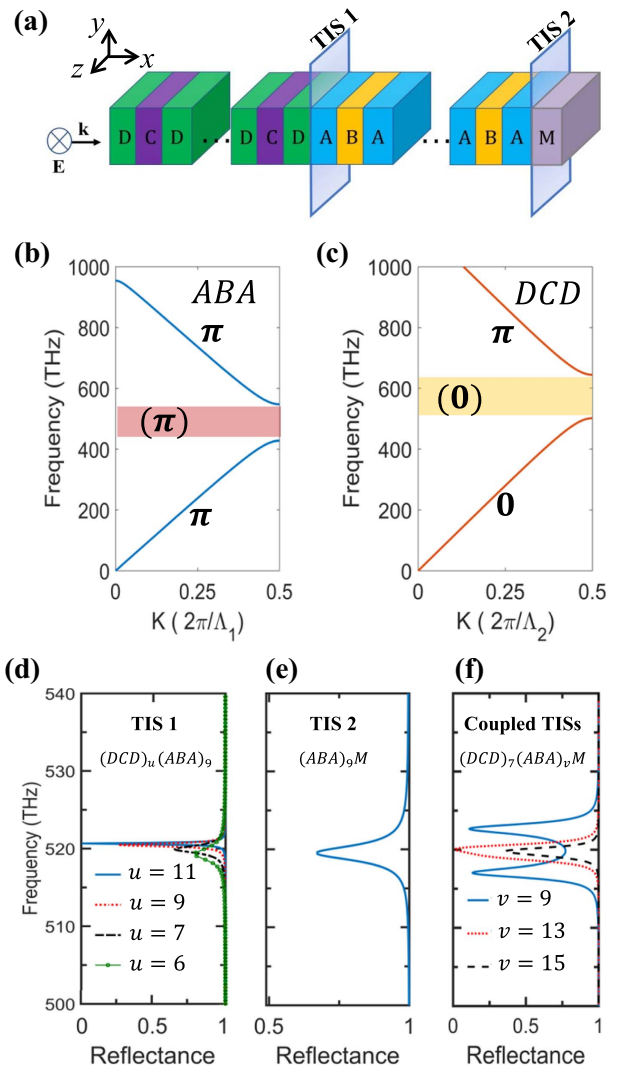

Fig. 1. (a) Schematic of sandwich structure $(DCD)_u(ABA)_vM$ with two coupled TISs. (b) Band structure of (ABA) PC. Red stripe represents the first bandgap with positive reflection phase. The Zak phase of each band is displayed next to it, and the sum of Zak phases below the first gap is shown in parentheses. (c) Band structure of (DCD) PC. Yellow stripe represents the first bandgap with negative reflection phase. (d) Reflectance for TIS 1 in $(DCD)_u(ABA)_9$. The blue solid, red dotted, black dashed, and green solid lines represent $u = 11$, 9, 7, and 6, respectively. (e) Reflectance for TIS 2 in $(ABA)_9M$. (f) Reflectance for coupled TISs in $(DCD)_7(ABA)_vM$. The blue solid, red dotted, and black dashed lines represent $v = 9$, 13, and 15, respectively.

are period numbers of ABA and DCD unit cells, respectively. The thicknesses of layers are designed to be $d_A = 32$ nm, $d_B = 120$ nm, $d_C = 64$ nm, $d_D = 44$ nm, and $d_M = 150$ nm, respectively. The lengths of two unit cells are $\Lambda_1 = 184$ nm and $\Lambda_2 = 152$ nm. The band structures of (ABA) PC (whose unit cell is ABA) and (DCD) PC (whose unit cell is DCD) with corresponding Zak phases are illustrated in Figs. 1(b) and 1(c), respectively. One can see that two PCs in the first gaps have different topological orders. According to "bulk-interface correspondence" [8], TIS 1 at the interface between two PCs must emerge within the overlapping

gap-frequency region (500–550 THz). Reflectance dips in Fig. 1(d) indicate that TIS 1 exists in $(DCD)_u(ABA)_9$. It is notable that the resonance frequency of TIS is slightly affected by the period number u when u is small, and it becomes independent of u when u is sufficiently large ($u > 9$). Similarly, for the TIS in $(DCD)_6(ABA)_v$, the frequency becomes independent of v when v is sufficiently large ($v > 9$).

TIS also exists at the interface between metal and PC, also known as Tamm plasma polaritons, as long as the reflection phases φ_{metal} and φ_{PC} satisfy $\varphi_{\text{metal}} + \varphi_{\text{PC}} = 0$ [2,11,64–67]. As indicated by the reflection dip in Fig. 1(e), TIS 2 emerges at the interface between the silver layer M with negative reflection phase and $(ABA)_v$ with positive reflection phase in the first bandgap. Here, a Lorentz–Drude model is used for the dielectric constant of silver in TMM calculation [68], and TIS 1 and TIS 2 are engineered to have nearly the same resonance frequency of $f = 519.8$ THz (corresponding vacuum wavelength is about 577 nm). The electric field distributions of two TISs are shown in Figs. 2(a) and 2(b), which clearly illustrate the strong localization of TISs.

Now we discuss coupled TISs in the sandwich structure $(DCD)_7(ABA)_vM$. As shown in Fig. 1(f), two dips in reflectance can be observed when $v = 9$, which indicates that the coupling of TISs leads to formation of two super-modes with different energies. Field distributions of the super-modes are shown in Figs. 2(c) and 2(d), where strong confinement of fields can be found near two interfaces. With the increase in period number v, the two super-modes gradually approach and merge at the critical coupling strength. To better show how v affects the coupling strength, the reflectance spectra for critical coupling ($v = 13$, red dotted line) and weak coupling ($v = 15$, black dashed line) are also given in Fig. 1(f). It is found that the reflection minimum increases with v for v greater than 13. The corresponding field distributions at resonance frequencies are shown in Figs. 2(e) and 2(f), respectively. It is seen that for v greater than 13, the field amplitude of TIS 2 decreases quickly with v, while for v less than 13, there is very little change in the field amplitude of TIS 2. These spectral responses, as well as field distributions, are closely related to the PT phase transition at critical coupling (EP), which will be discussed in detail in the next section.

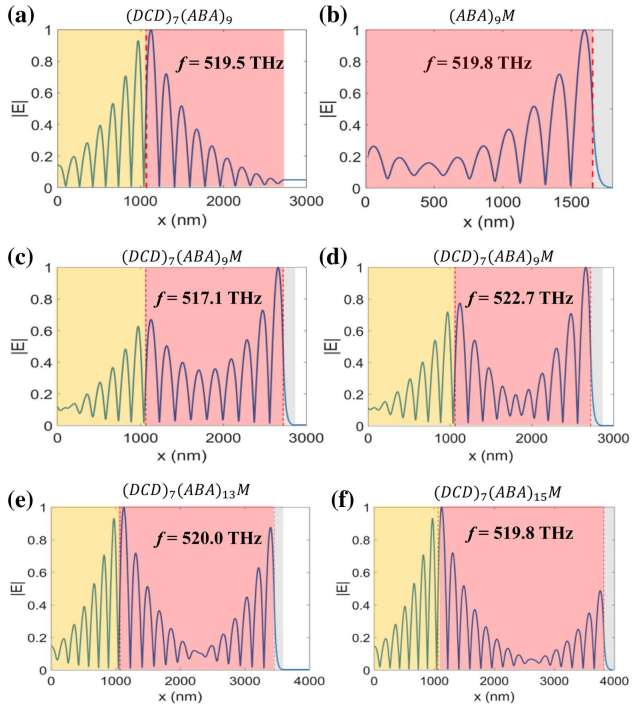

Fig. 2. Distribution of normalized electric field amplitude for different topological states. The yellow, red, gray, and white shaded areas represent the photonic crystal DCD, ABA, silver, and air background, respectively. (a) TIS 1 in $(DCD)_7(ABA)_9$. (b) TIS 2 in $(ABA)_9M$. (c), (d) Super-modes with (c) lower and (d) higher energy in $(DCD)_7(ABA)_9M$ with strong coupling. (e) Merged TISs in $(DCD)_7(ABA)_{13}M$ with critical coupling. (f) Merged TISs in $(DCD)_7(ABA)_{13}M$ with weak coupling. The red dashed lines represent the interfaces between different PCs and metal.

Spectral responses of the aforementioned structures can be well explained by CMT, and a PT-symmetric system can be achieved based on the analysis of CMT. Here, a TIS can be regarded as resonance mode $\tilde{a}_0 = a_0 e^{-i\omega t}$, and the dynamic equation for a single resonance mode with single-port excitation based on the Lorentz model can be written as [69]

$$\frac{d\tilde{a}_0}{dt} = (-i\omega_0 - \gamma_{01} - \gamma_{02} - \Gamma)\tilde{a}_0 + \sqrt{2\gamma_{01}} S_{1+} e^{-i\omega t}, \tag{1}$$

where ω_0, Γ, and S_{1+} are the resonance frequency, intrinsic loss, and amplitude of the input wave at port 1, respectively. γ_{01} (γ_{02}) denotes scattering loss, which is determined by the coupling between TIS and input port 1 (output port 2). The reflection coefficient at port 1 is

$$r = -1 + \frac{\sqrt{2\gamma_{01}} a_0}{S_{1+}} = -1 + \frac{2i\gamma_{01}}{(\omega - \omega_0) + i(\gamma_{01} + \gamma_{02} + \Gamma)}. \tag{2}$$

The dynamic equations for coupled TISs in a sandwich structure ($\tilde{a}_1 = a_1 e^{-i\omega t}$, $\tilde{a}_2 = a_2 e^{-i\omega t}$) can be described by CMT as follows [70]:

$$\frac{d\tilde{a}_1}{dt} = (-i\omega_{01} - \gamma_1 - \Gamma_1)\tilde{a}_1 - i\kappa\tilde{a}_2 + \sqrt{2\gamma_1} S_{1+} e^{-i\omega t}, \tag{3}$$

$$\frac{d\tilde{a}_2}{dt} = (-i\omega_{02} - \gamma_2 - \Gamma_2)\tilde{a}_2 - i\kappa\tilde{a}_1, \tag{4}$$

where κ denotes the coupling rate between TISs $\tilde{a}_1$ and $\tilde{a}_2$; γ_1 (γ_2) denotes the coupling rate between TIS 1 (TIS 2) and port 1 (port 2). Γ_1 (Γ_2) denotes intrinsic loss. ω_{01} and ω_{02} denote resonance frequencies of TIS 1 and TIS 2, respectively. Here, for the chosen parameters, we have $\omega_{01} = \omega_{02} = \omega_0$. From the equations above, the reflection coefficient can be written as

$$r = -1 + \frac{\sqrt{2\gamma_1} a_1}{S_{1+}}. \tag{5}$$

Considering the zero-reflection case $r = 0$, we obtain an eigenvalue equation from Eqs. (3) and (4) as

$$H \begin{bmatrix} a_1 \\ a_2 \end{bmatrix} = \omega \begin{bmatrix} a_1 \\ a_2 \end{bmatrix}, \tag{6}$$

where

$$H = \begin{pmatrix} \omega_0 + i(\gamma_1 - \Gamma_1) & \kappa \\ \kappa & \omega_0 - i(\gamma_2 + \Gamma_2) \end{pmatrix}. \quad (7)$$

The eigenvalues of H are

$$\omega_\pm = \omega_0 + i\frac{(\gamma_1 - \Gamma_1) - (\gamma_2 + \Gamma_2)}{2} \pm \sqrt{\kappa^2 - \left(\frac{(\gamma_1 - \Gamma_1) + (\gamma_2 + \Gamma_2)}{2}\right)^2}. \quad (8)$$

It can be concluded that H represents the effective Hamiltonian of the sandwich structure, in which γ_1 can be regarded as an effective gain. The Hamiltonian becomes ideal PT symmetric when satisfying $\gamma_1 - \Gamma_1 = \gamma_2 + \Gamma_2$ [61].

3. PERFECT LIGHT ABSORBER VIA COUPLED TISS WITH IDEAL PT SYMMETRY

Now we focus on the design of a PT-symmetric photonic structure with coupled TISs to realize perfect absorption. First, the model parameters in the effective Hamiltonian H, which can be engineered by altering period numbers u and v, are extracted from fitting the spectral response with CMT. For the selected sandwich structure $(DCD)_6(ABA)_pM$, the coupling rate between port 1 and TIS 1 (denoted as γ_1) and intrinsic loss of TIS 2 (denoted as Γ_2) can be obtained independently from the resonance spectra of structures $(DCD)_6(ABA)_{10}$ and $(ABA)_{10}M$. As shown in Figs. 3(a) and 3(b), within the interested frequency region, TMM-based calculation for the reflectance spectra of two TIS resonances in $(DCD)_6(ABA)_{10}$ and $(ABA)_{10}M$ can be well fitted using the Lorentz model in Eq. (2). Here, γ_{L1} (γ_{L2}) denotes the coupling rate between TIS 1 and port 1 (port 2) in $(DCD)_6(ABA)_{10}$. γ_{R1} (γ_{R2}) denotes the coupling rate between TIS 2 and port 1 (port 2) in $(ABA)_{10}M$. Γ_L (Γ_R) denotes intrinsic loss of TIS 1 (TIS 2). Hence the model parameters for $(DCD)_6(ABA)_pM$ are derived as follows: $\omega_{01} = \omega_{02} = \omega_0 = 2\pi f_0$, $f_0 = 519.2$ THz ($\lambda_0 = 577.8$ nm), $\gamma_1/2\pi = \gamma_{L1}/2\pi = 1.126$ THz, $\gamma_2 = \gamma_{R2} = 0$ (thickness of the silver layer is $d_M = 150$ nm, which is thick enough to ensure TIS 2 is isolated from port 2), $\Gamma_1 = \Gamma_L = 0, \Gamma_2/2\pi = \Gamma_R/2\pi = 1.085$ THz. Specific methods to obtain these model parameters are given in Appendix A. It is obvious that the ideal PT symmetry condition ($\gamma_1 - \Gamma_1 = \gamma_2 + \Gamma_2$) is almost satisfied in this design ($u = 6$). Further, by fitting the reflectance of the sandwich structure for different period numbers p ($p = 9, 10, \ldots, 14$), the relation between $|\kappa|$ and p is obtained as $|\kappa|/2\pi = 63.06 \cdot \exp(-0.341p)$ THz.

Then the eigenvalue spectra of the effective Hamiltonian H versus $|\kappa|$ can be calculated from Eq. (8) and are shown in Fig. 4(a) with red solid (real part) and black dashed (imaginary part) lines. The eigenvalues are a pair of conjugated complex numbers with weak coupling ($|\kappa|/2\pi < 1.1$ THz), while with strong coupling ($|\kappa|/2\pi > 1.1$ THz), the eigenvalues are two real numbers, which means that this ideal PT-symmetric non-Hermitian system has pseudo-Hermiticity in the PT-unbroken phase [71]. The case with $p = 12$ is found to be very close to the phase transition EP ($|\kappa|/2\pi = 1.1$ THz), at which two eigenvalues coalesce.

TMM-based calculation for the absorption spectra of $(DCD)_6(ABA)_pM$ with different p as well as the corresponding well-fitted CMT results is given in Fig. 5. According to analysis in Section 2, the frequencies of perfect absorption peaks can be regarded as real eigenvalues of the effective Hamiltonian H. Hence, the PT phase transition in Fig. 4(a) can be demonstrated clearly in these absorption spectra. In Fig. 5(a), two perfect absorption peaks indicating a PT-symmetric phase can be found in a relatively strong coupling regime ($p = 9$). With the decrease in coupling rate, the frequencies of absorption peaks gradually get close to each other, which can be

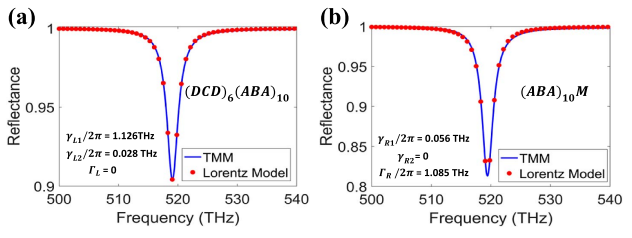

Fig. 3. (a) Reflectance spectra of TIS 1 in $(DCD)_6(ABA)_{10}$ calculated by TMM (blue solid line) and Lorentz model (red hexagonal points). (b) Same as in (a), but for TIS 2 in $(ABA)_{10}M$.

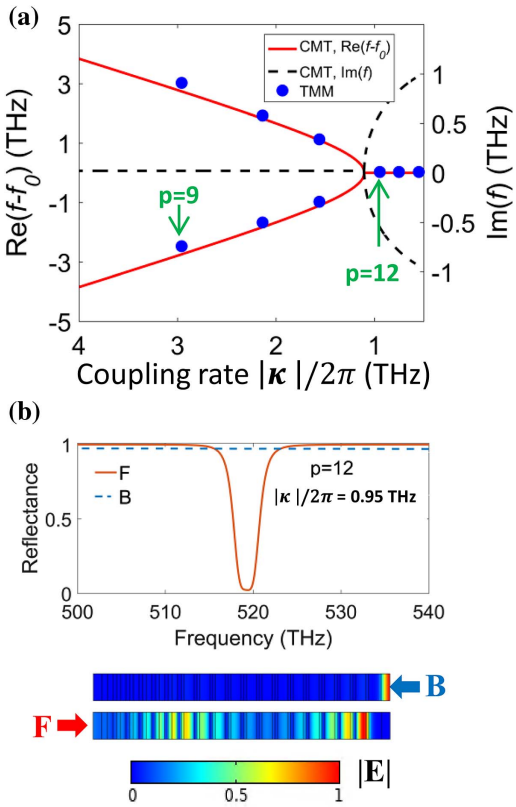

Fig. 4. (a) Eigenvalue spectra of effective PT-symmetric system $[(DCD)_6(ABA)_pM]$ versus coupling rate $|\kappa|$ (period number p) between two TISs. Blue circles represent absorption peaks with varied period numbers p. (b) Reflectance and normalized electric field distribution of system for forward (F)/backward (B) propagation with $p = 12$. Red/blue line stands for forward/backward propagation. The layers at two ends are air layers.

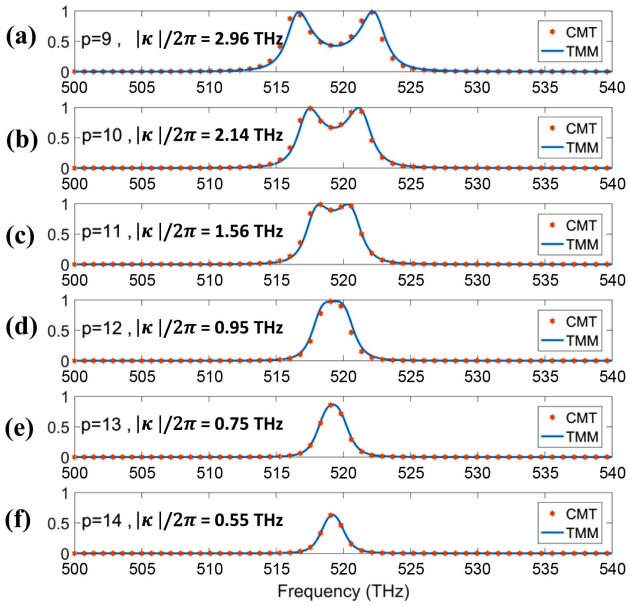

Fig. 5. Calculated absorption spectra of $(DCD)_6(ABA)_pM$ with different period numbers p by using TMM (blue solid line) and CMT (red hexagonal points).

seen in Figs. 5(b) and 5(c) for the cases of $p = 10, 11$. They merge in the vicinity of f_0 in the case of $p = 12$, indicating the existence of EP. In the cases of $p = 13, 14$, the peak value of the absorption peak gradually decreases as p increases, as shown in Figs. 5(e) and 5(f). In these cases, the system gets into the PT-broken phase. With the imaginary part of the eigenvalue increasing, the reflectance caused by mode-mismatch also increases, so the absorption drops accordingly. The frequencies of these absorption peaks from TMM with varying p are illustrated in Fig. 4(a) with blue circles, which further indicates the PT phase transition.

It is worth noting that perfect absorption peaks in Figs. 5(a)–5(d) all satisfy the condition $R_{\text{left}} = 0$, $R_{\text{right}} \neq 0$ (R represents reflectance, subscript left stands for left incidence, and right stands for right incidence), which resembles unidirectional invisibility discovered in modulated PT-symmetric waveguides [31]. Here, unidirectional invisibility in structure $(DCD)_6(ABA)_{12}M$ is visualized in Fig. 4(b). Light incident from the left side can go through the structure without reflection at ω_0, while light incident from the right side is totally reflected. The resulted asymmetric field distributions for left and right incidences are given in the bottom panel of Fig. 4(b). The reflectance is not precisely zero because the case of $p = 12$ deviates a little bit from exact EP ($|\kappa|/2\pi = 1.1$ THz), which can be seen in Fig. 4(a).

4. LIGHT ABSORBER VIA COUPLED TISS WITH NON-IDEAL PT SYMMETRY

The number of layers involved in the aforementioned structure is too large, so it is difficult to fabricate the structure with high accuracy. For such a multilayer film prepared by electron beam evaporation, the thicker the total structure becomes, the more likely fabrication error will be introduced, which will eventually lead to the failure of the experiment. To solve the problem, we substitute the PC $(DCD)_6$ for a coated silver layer so that total thickness of the sample can be greatly reduced. Here, the reflection phase of coated silver layer φ'_{metal} is negative, so TIS 1 can still be achieved according to the existence condition of TIS $\varphi'_{\text{metal}} + \varphi_{ABA} = 0$.

But now there is another problem: loss and effective gain are not exactly balanced in the proposed new structure. Fortunately, the PT phase transition can still be observed in a system with unbalanced loss and gain [72]. So finally, we design a non-ideal PT-symmetric (also called gauged PT) structure that is possible to achieve in the experiment.

The considered non-ideal PT-symmetric structure, namely, $(D'C'D')M'(A'B'A')_qM$, which support two TISs at both ends of $(A'B'A')_q$, is shown in Fig. 6(a). The thicknesses of dielectric layers are designed to be $d_{A'} = 32$ nm, $d_{B'} = 60$ nm, $d_{C'} = 50$ nm, and $d_{D'} = 65$ nm (here, we adjust the thickness of layer B a bit to further reduce total thickness). The thicknesses of silver layers adjacent to the left/right boundaries of PC $(A'B'A')_q$ are $d_{M'} = 24$ nm and $d_M = 120$ nm, respectively. Also, one unit cell of $D'C'D'$ acts as a coating layer to protect silver from air. Similar to the previous design, the two TISs are first investigated in the separated structures, i.e., $(D'C'D')M'(A'B'A')_{10}$ and $(A'B'A')_{10}M$, as given in Figs. 6(b) and 6(c), respectively. The corresponding field enhancements are verified in Figs. 6(d) and 6(e). It must be

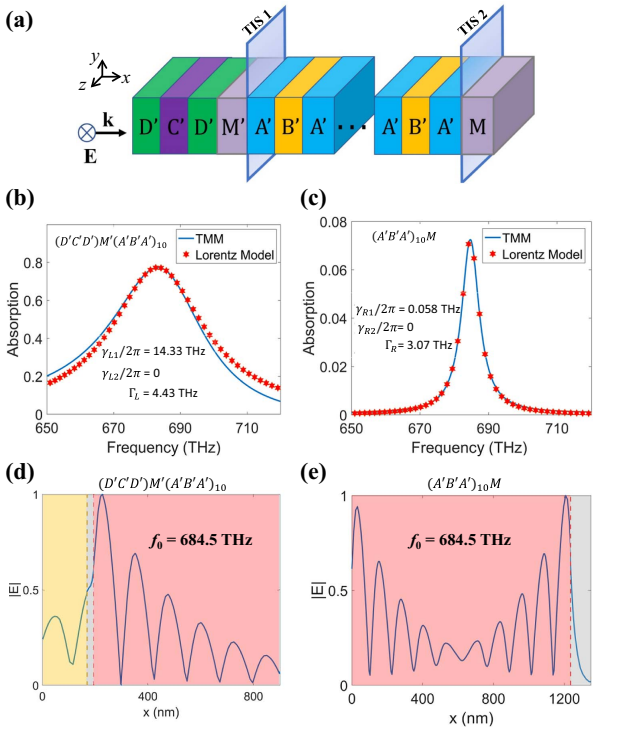

Fig. 6. (a) Schematic of PC heterostructure $(D'C'D')M'(A'B'A')_qM$. (b), (c) Calculated absorption spectra of (b) TIS 1 in $(D'C'D')M'(A'B'A')_{10}$ and (c) TIS 2 in $(A'B'A')_{10}M$, using TMM (blue solid line) and Lorentz model (red hexagonal points). (d), (e) Corresponding distribution of normalized electric field amplitude. The yellow (red) dashed line represents the interface between silver layers M' and D' (A').

pointed out that there is no interface state on the interface between silver M' and $D'C'D'$ [this interface is denoted by the yellow dashed line in Fig. 6(d)], as M' and $D'C'D'$ are topologically indistinguishable in the interested gap-frequency region. A little asymmetry for the line shape in Fig. 6(b) may result from dispersion of the thin silver layer. Nevertheless, the Lorentz model is sufficient enough for us to acquire the scattering loss γ and intrinsic loss Γ of the resonance. For these new samples, using the same method in the ideal PT symmetry case, we have $\omega_{01} = \omega_{02} = 2\pi f_0$, $f_0 = 684.5$ THz ($\lambda_0 = 438.3$ nm), and the other fitted parameters are: $\gamma_1/2\pi = \gamma_{L1}/2\pi = 14.33$ THz, $\gamma_2 = \gamma_R = 0$, $\Gamma_1/2\pi = \Gamma_L/2\pi = 4.43$ THz, $\Gamma_2/2\pi = \Gamma_R/2\pi = 3.07$ THz, as shown in Figs. 6(b) and 6(c). In addition, the dependence of coupling rate $|\kappa|$ on period number q ($q = 6, 7, \ldots, 12$) is $|\kappa|/2\pi = 137.88\exp(-0.373q)$ THz.

Although the ideal PT symmetry condition is not satisfied for $(D'C'D')M'(A'B'A')_qM$, we will show that a PT phase transition and one-channel CPA can still be demonstrated in the following. The eigenvalues calculated by CMT together with absorption peaks extracted from TMM are shown in Fig. 7(a). The system is found to be working in the vicinity of a real eigenvalue when $q = 9$, leading to nearly perfect absorption at $f_0 = 684.5$ THz. This eigenvalue can be seen as one-cannel CPA in the PT symmetry broken phase, as shown in Fig. 7(a). It should be pointed out that in Fig. 7(a), EP is reached between $q = 8$ and $q = 9$ with a non-zero imaginary part [$\mathrm{Im}(\omega) = 3.27$]. Absorption spectra calculated by TMM and CMT are also given in Fig. 7(c). Two absorption peaks (671.9, 698.5 THz) with peak values less than one (about 0.90) are observed when the system is in the unbroken phase before EP ($q = 6$). In the case of $q = 9$, only one (nearly perfect) absorption peak of 0.99 can be found at f_0, indicating one-channel CPA. It should be pointed out that perfect absorption with broken PT symmetry is also achieved in a metasurface system [73]. With the increase in period number q, absorption decreases from 0.99 to 0.80 at $q = 12$, while the frequency of the peak remains unchanged. Such merging in absorption peaks illustrates the PT phase transition in the non-ideal case. Particularly, the system can have a real eigenvalue at the critical coupling of $|\kappa|/2\pi = 5.64$ THz (approximately $q = 9$) in the PT broken phase. It means proper coupling may result in pseudo-Hermiticity of a non-ideal PT-symmetric system.

Finally, we fabricate the structures $(D'C'D')M'(A'B'A')_6M$ discussed above and conduct the experiment. The sample is evaporated on the substrate BK7 with a refractive index of 1.51 by electron beam evaporation. The Nova NanoSEM 450 scanning electron microscopy image of the case of $q = 6$ as an example is shown in Fig. 7(b). The reflectance R as well as transmittance T is measured using a Perkin Elmer LAMBDA 1050 WB ultraviolet-visible-near-infrared spectrophotometer, and the absorption spectra are calculated through the relation absorption $= 1 - R - T$, shown in Fig. 7(d).

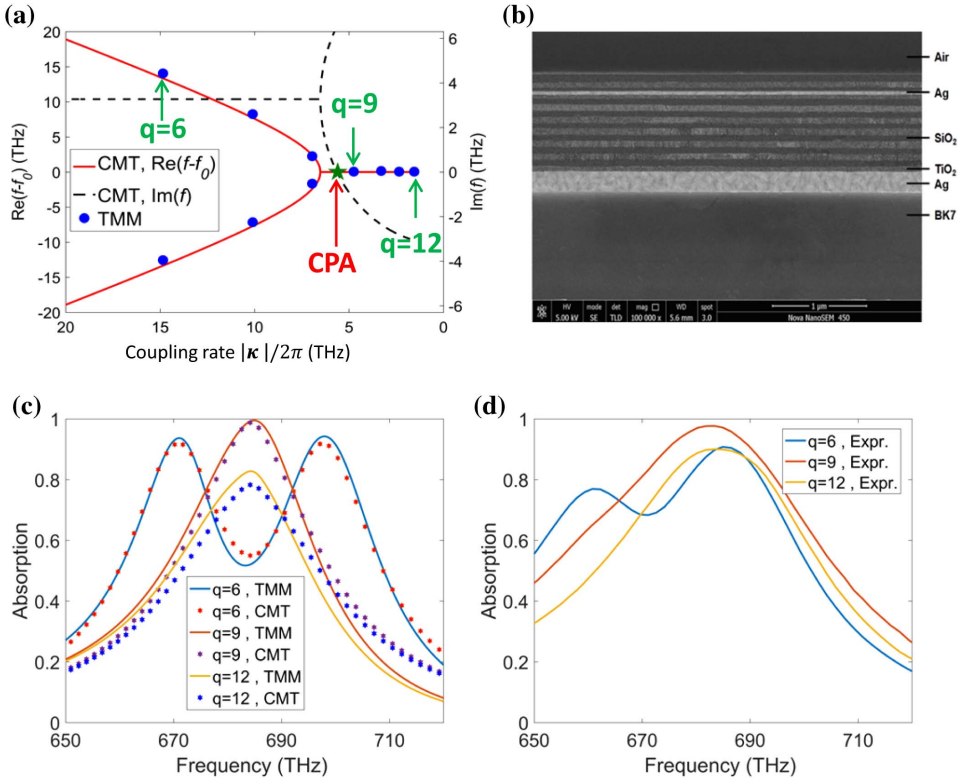

Fig. 7. (a) Eigenvalue spectra of non-ideal PT symmetric system $[(D'C'D')M'(A'B'A')_qM]$ versus different coupling rates $|\kappa|$ (period number q). Blue circles represent absorption peaks of the system with varied period numbers $q = 6$–12 calculated by TMM. Green star represents the case where the Hamiltonian of the system has a real eigenvalue (one-channel CPA is achieved). (b) SEM image of one sample of $q = 6$. (c) Absorption spectra calculated from TMM (solid lines) and CMT (hexagonal dots). (d) Measured absorption spectra.

As shown in Fig. 7(d), the evolution of the absorption spectrum unique to non-ideal PT symmetry is measured in experiments. First, under strong coupling, two absorption peaks (660.8, 684.9 THz) are observed in the case of $q = 6$ (bule line). In the case of $q = 9$ (red line), which is approximately under critical coupling, only one nearly perfect absorption peak of 0.98 appears at $f = 683.4$ THz. It is very consistent with the simulated resonance frequency $f_0 = 684.5$ THz ($\lambda_0 = 438.3$ nm). As the period number q increases further, the measured peak absorption drops from 0.98 to 0.90 at $q = 12$ (yellow line), while the frequency of the peak remains unchanged at $\omega = 683.4$ THz. The measured absorption spectrum is reasonably consistent with the calculation in Fig. 7(c). Small deviation (less than 2%) of the resonance frequency in the case of $q = 6$ is mainly caused by errors in refractive index discrepancies between the experimental materials and simulated values and layer thickness monitoring errors during the deposition process. Nevertheless, the PT phase transition and perfect light absorber are clearly demonstrated in experiments.

5. CONCLUSION

In conclusion, we propose an optical PT-symmetric scheme to realize a perfect light absorber based on the coupling of TISs in PCs. The PT phase transition is achieved in both ideal and non-ideal PT symmetry cases. In the ideal PT symmetry case, one-channel CPA with unidirectional invisibility at EP is numerically obtained. In the non-ideal case, one-channel CPA in the broken phase is observed experimentally. Our work demonstrates the possibility of manipulating non-Hermiticity of a PT system by tuning the coupling rate of TISs. The results facilitate the design of EP-based functional devices, such as unidirectional light absorbers, EP sensors, and nonlinear devices.

APPENDIX A: SPECIFIC METHODS TO OBTAIN MODEL PARAMETERS

The model parameters for a single TIS are obtained by fitting the reflectance spectra (calculated by TMM) with the Lorentz model in Eq. (2). In detail, we first acquire the resonance frequency ω_0, reflectance at ω_0 (reflectance dip), and half-width of TIS resonance X from the reflectance spectrum. These parameters together with $\gamma_{01}, \gamma_{02}, \Gamma$ are all real quantities. According to the standard Lorentz model in Eq. (2), we have

$$R(\omega_0) = |r(\omega_0)|^2 = \left(-1 + \frac{2\gamma_{01}}{X}\right)^2, \tag{A1}$$

$$X = \gamma_{01} + \gamma_{02} + \Gamma. \tag{A2}$$

So we have the following equation for the model parameter:

$$\gamma_{01} = \frac{X}{2}\left(1 \pm \sqrt{R(\omega_0)}\right). \tag{A3}$$

The signs (positive and negative) in Eq. (A3) are determined by the relative values of γ_{01} and γ_{02} (Γ). For the structure $(DCD)_u(ABA)_{10}$ in Fig. 3(a), where $\Gamma = 0$, when $\gamma_{01} = \gamma_{02}$, we have $R = 0$. The period number of DCD with which $R = 0$ is satisfied can be denoted as u_0. If $u < u_0$, there must be $\gamma_{01} > \gamma_{02}$ because γ_{01} increases as u decreases. We find that when $u = 13$, the value of reflectance $R(\omega_0)$ is near zero. Therefore, for $u < u_0 = 13$, we always have $\gamma_{01} > \gamma_{02}$. For $\gamma_{01} > \gamma_{02}$, we have $\gamma_{01} = X(1 + \sqrt{R(\omega_0)})/2$ and $\gamma_{02} = X - \gamma_{01}$.

For the structure $(ABA)_vM$ in Fig. 3(b), where $\gamma_{02} = 0$, when $\gamma_{01} = \Gamma$, we have $R = 0$. The period number of ABA with which $R = 0$ is satisfied can be denoted as v_0. If $v > v_0$, there must be $\gamma_{01} < \Gamma$ because γ_{01} decreases as v increases. We find that when $v = 6$, the value of reflectance $R(\omega_0)$ is near zero. Therefore, for $v > v_0 = 6$, we always have $\gamma_{01} < \Gamma$. For $\gamma_{01} < \Gamma$, we have $\gamma_{01} = X(1 - \sqrt{R(\omega_0)})/2$ and $\Gamma = X - \gamma_{01}$.

Funding. National Key Research and Development Program of China (2021YFA1400602); National Natural Science Foundation of China (11974261, 12275161, 61621001, 62075213, 91850206); Fundamental Research Funds for the Central Universities (22120190222).

Disclosures. The authors declare no conflicts of interest.

Data Availability. Data underlying the results presented in this paper are not publicly available at this time but may be obtained from the authors upon reasonable request.

REFERENCES

1. A. V. Kavokin, I. A. Shelykh, and G. Malpuech, "Lossless interface modes at the boundary between two periodic dielectric structures," Phys. Rev. B **72**, 233102 (2005).
2. M. Kaliteevski, I. Iorsh, S. Brand, R. A. Abram, J. M. Chamberlain, A. V. Kavokin, and I. A. Shelykh, "Tamm plasmon-polaritons: possible electromagnetic states at the interface of a metal and a dielectric Bragg mirror," Phys. Rev. B **76**, 165415 (2007).
3. N. Malkova, I. Hromada, X. Wang, G. Bryant, and Z. Chen, "Transition between Tamm-like and Shockley-like surface states in optically induced photonic superlattices," Phys. Rev. A **80**, 043806 (2009).
4. N. Malkova, I. Hromada, X. Wang, G. Bryant, and Z. Chen, "Observation of optical Shockley-like surface states in photonic superlattices," Opt. Lett. **34**, 1633–1635 (2009).
5. F. Gao, Z. Gao, X. Shi, Z. Yang, X. Lin, H. Xu, J. D. Joannopoulos, M. Soljačić, H. Chen, L. Lu, Y. Chong, and B. Zhang, "Probing topological protection using a designer surface plasmon structure," Nat. Commun. **7**, 11619 (2016).
6. C. F. Fan, X. Shi, F. Wu, Y. H. Li, H. T. Jiang, Y. Sun, and H. Chen, "Photonic topological transition in dimerized chains with the joint modulation of near-field and far-field couplings," Photon. Res. **10**, 41–49 (2022).
7. R. D. King-Smith and D. Vanderbilt, "Theory of polarization of crystalline solids," Phys. Rev. B **47**, 1651–1654 (1993).
8. M. Xiao, Z. Q. Zhang, and C. T. Chan, "Surface impedance and bulk band geometric phases in one-dimensional systems," Phys. Rev. X **4**, 021017 (2014).
9. A. Alù and N. Engheta, "Pairing an Epsilon-negative slab with a mu-negative slab: resonance, tunneling and transparency," IEEE Trans. Antennas Propag. **51**, 2558–2571 (2003).
10. H. T. Jiang, H. Chen, H. Q. Li, Y. W. Zhang, J. Zi, and S. Y. Zhu, "Properties of one-dimensional photonic crystals containing single-negative materials," Phys. Rev. E **69**, 066607 (2004).
11. J. Y. Guo, Y. Sun, Y. W. Zhang, H. Q. Li, H. T. Jiang, and H. Chen, "Experimental investigation of interface states in photonic crystal heterostructures," Phys. Rev. E **78**, 026607 (2008).
12. T. Goto, A. V. Dorofeenko, A. M. Merzlikin, A. V. Baryshev, A. P. Vinogradov, M. Inoue, A. A. Lisyansky, and A. B. Granovsky,

"Optical Tamm states in one-dimensional magnetophotonic structures," Phys. Rev. Lett. **101**, 113902 (2008).
13. W. Tan, Y. Sun, H. Chen, and S. Q. Shen, "Photonic simulation of topological excitations in metamaterials," Sci. Rep. **4**, 3842 (2014).
14. X. Shi, C. H. Xue, H. T. Jiang, and H. Chen, "Topological description for gaps of one-dimensional symmetric all-dielectric photonic crystals," Opt. Express **24**, 18580–18591 (2016).
15. Y. M. Qing, H. F. Ma, L. W. Wu, and T. J. Cui, "Manipulating the light-matter interaction in a topological photonic crystal heterostructure," Opt. Express **28**, 34904–34915 (2020).
16. J. Wu and Y. M. Qing, "Strong nonreciprocal radiation with topological photonic crystal heterostructure," Appl. Phys. Lett. **121**, 112201 (2022).
17. H. Lu, C. H. Xue, Y. G. Wu, S. Q. Chen, X. L. Zhang, H. T. Jiang, J. G. Tian, and H. Chen, "Enhanced nonlinear optical response of a planar thick metal film combined with a truncated photonic crystal," Opt. Commun. **285**, 5416–5419 (2012).
18. X. Wang, Y. Liang, L. Wu, J. Guo, X. Dai, and Y. Xiang, "Multi-channel perfect absorber based on a one-dimensional topological photonic crystal heterostructure with graphene," Opt. Lett. **43**, 4256–4259 (2018).
19. K. Zhang, F. Xia, S. Li, Y. Liu, and W. Kong, "Actively tunable multi-band terahertz perfect absorber due to the hybrid strong coupling in the multilayer structure," Opt. Express **29**, 28619–28630 (2021).
20. J. Hu, W. Liu, W. Xie, W. Zhang, E. Yao, Y. Zhang, and Q. Zhan, "Strong coupling of optical interface modes in a 1D topological photonic crystal heterostructure/Ag hybrid system," Opt. Lett. **44**, 5642–5645 (2019).
21. M. Y. Hu, K. Ding, T. Qiao, X. Jiang, Q. Wang, S. Zhu, and H. Liu, "Realization of photonic charge-2 Dirac point by engineering supermodes in topological superlattices," Commun. Phys. **3**, 130 (2020).
22. C. M. Bender and S. Boettcher, "Real spectra in non-Hermitian Hamiltonians having parity-time symmetry," Phys. Rev. Lett. **80**, 5243–5246 (1998).
23. R. El-Ganainy, K. G. Makris, M. Khajavikhan, Z. H. Musslimani, S. Rotter, and D. N. Christodoulides, "Non-Hermitian physics and PT symmetry," Nat. Phys. **14**, 11–19 (2018).
24. L. Feng, R. El-Ganainy, and L. Ge, "Non-Hermitian photonics based on parity-time symmetry," Nat. Photonics **11**, 752–762 (2017).
25. R. Fleury, D. Sounas, and A. Alu, "An invisible acoustic sensor based on parity-time symmetry," Nat. Commun. **6**, 5905 (2015).
26. S. Assawaworrarit and S. Fan, "Robust and efficient wireless power transfer using a switch-mode implementation of a nonlinear parity–time symmetric circuit," Nat. Electron. **3**, 273–279 (2020).
27. Z. Y. Zhang, Y. Q. Zhang, J. T. Sheng, L. Yang, M. A. Miri, D. N. Christodoulides, B. He, Y. P. Zhang, and M. Xiao, "Observation of parity-time symmetry in optically induced atomic lattices," Phys. Rev. Lett. **117**, 123601 (2016).
28. A. Guo, G. J. Salamo, D. Duchesne, R. Morandotti, M. Volatier-Ravat, V. Aimez, G. A. Siviloglou, and D. N. Christodoulides, "Observation of PT-symmetry breaking in complex optical potentials," Phys. Rev. Lett. **103**, 093902 (2009).
29. C. E. Rüter, K. G. Makris, R. El-Ganainy, D. N. Christodoulides, M. Segev, and D. Kip, "Observation of parity-time symmetry in optics," Nat. Phys. **6**, 192–195 (2010).
30. B. Peng, S. K. Ozdemir, S. Rotter, H. Yilmaz, M. Liertzer, F. Monifi, C. M. Bender, F. Nori, and L. Yang, "Loss-induced suppression and revival of lasing," Science **346**, 328–332 (2014).
31. L. Feng, M. Ayache, J. Q. Huang, Y. L. Xu, M. H. Lu, Y. F. Chen, Y. Fainman, and A. Scherer, "Nonreciprocal light propagation in a silicon photonic circuit," Science **333**, 729–733 (2011).
32. Z. Lin, H. Ramezani, T. Eichelkraut, T. Kottos, H. Cao, and D. N. Christodoulides, "Unidirectional invisibility induced by PT-symmetric periodic structures," Phys. Rev. Lett. **106**, 213901 (2011).
33. A. Regensburger, C. Bersch, M. A. Miri, G. Onishchukov, D. N. Christodoulides, and U. Peschel, "Parity-time synthetic photonic lattices," Nature **488**, 167–171 (2012).
34. R. Fleury, D. Sounas, and A. Alu, "Negative refraction and planar focusing based on parity-time symmetric metasurfaces," Phys. Rev. Lett. **113**, 023903 (2014).
35. S. Longhi, "PT-symmetric laser absorber," Phys. Rev. A **82**, 031801 (2010).
36. Y. Sun, W. Tan, H. Q. Li, J. Li, and H. Chen, "Experimental demonstration of a coherent perfect absorber with PT phase transition," Phys. Rev. Lett. **112**, 143903 (2014).
37. K. Ding, G. Ma, M. Xiao, Z. Q. Zhang, and C. T. Chan, "Emergence, coalescence, and topological properties of multiple exceptional points and their experimental realization," Phys. Rev. X **6**, 021007 (2016).
38. M.-A. Miri and A. Alù, "Exceptional points in optics and photonics," Science **363**, eaar7709 (2019).
39. S. K. Özdemir, S. Rotter, F. Nori, and L. Yang, "Parity–time symmetry and exceptional points in photonics," Nat. Mater. **18**, 783–798 (2019).
40. H. Hodaei, M. A. Miri, M. Heinrich, D. N. Christodoulides, and M. Khajavikhan, "Parity-time-symmetric microring lasers," Science **346**, 975–978 (2014).
41. H. Hodaei, M. A. Miri, A. U. Hassan, W. E. Hayenga, M. Heinrich, D. N. Christodoulides, and M. Khajavikhan, "Single mode lasing in transversely multi-moded PT-symmetric microring resonators," Laser Photon. Rev. **10**, 494–499 (2016).
42. P. Miao, Z. F. Zhang, J. B. Sun, W. Walasik, S. Longhi, N. M. Litchinitser, and L. Feng, "Orbital angular momentum microlaser," Science **353**, 464–467 (2016).
43. J. Wiersig, "Enhancing the sensitivity of frequency and energy splitting detection by using exceptional points: application to microcavity sensors for single particle detection," Phys. Rev. Lett. **112**, 203901 (2014).
44. H. Hodaei, A. U. Hassan, S. Wittek, H. Garcia-Gracia, R. El-Ganainy, D. N. Christodoulides, and M. Khajavikhan, "Enhanced sensitivity at higher-order exceptional points," Nature **548**, 187–191 (2017).
45. J. Wiersig, "Review of exceptional point-based sensors," Photon. Res. **8**, 1457–1467 (2020).
46. W. Chen, S. K. Özdemir, G. Zhao, J. Wiersig, and L. Yang, "Exceptional points enhance sensing in an optical microcavity," Nature **548**, 192–196 (2017).
47. P.-Y. Chen, M. Sakhdari, M. Hajizadegan, Q. Cui, M. M.-C. Cheng, R. El-Ganainy, and A. Alú, "Generalized parity-time symmetry condition for enhanced sensor telemetry," Nat. Electron. **1**, 297 (2018).
48. Z. Dong, Z. Li, F. Yang, C. Qiu, and J. Ho, "Sensitive readout of implantable microsensors using a wireless system locked to an exceptional point," Nat. Electron. **2**, 335 (2019).
49. J. M. P. Nair, D. Mukhopadhyay, and G. S. Agarwal, "Enhanced sensing of weak anharmonicities through coherences in dissipatively coupled anti-PT symmetric systems," Phys. Rev. Lett. **126**, 180401 (2021).
50. C. Q. Wang, W. R. Sweeney, A. D. Stone, and L. Yang, "Coherent perfect absorption at an exceptional point," Science **373**, 1261–1265 (2021).
51. S. Y. Yao and Z. Wang, "Edge states and topological invariants of non-Hermitian systems," Phys. Rev. Lett. **121**, 086803 (2018).
52. W. G. Song, W. Z. Sun, C. Chen, Q. H. Song, S. M. Xiao, S. Zhu, and T. Li, "Breakup and recovery of topological zero modes in finite non-Hermitian optical lattices," Phys. Rev. Lett. **123**, 165701 (2019).
53. S. Xia, D. Kaltsas, D. Song, I. Komis, J. Xu, A. Szameit, H. Buljan, K. G. Makris, and Z. Chen, "Nonlinear tuning of PT symmetry and non-Hermitian topological states," Science **372**, 72–76 (2021).
54. A. U. Hassan, B. Zhen, M. Soljačić, M. Khajavikhan, and D. N. Christodoulides, "Dynamically encircling exceptional points: exact evolution and polarization state conversion," Phys. Rev. Lett. **118**, 093002 (2017).
55. X. L. Zhang, S. Wang, B. Hou, and C. T. Chan, "Dynamically encircling exceptional points: *in situ* control of encircling loops and the role of the starting point," Phys. Rev. X. **8**, 021066 (2018).
56. Z. W. Guo, J. Jiang, H. T. Jiang, J. Ren, and H. Chen, "Observation of topological bound states in a double Su-Schrieffer-Heeger chain composed of split ring resonators," Phys. Rev. Res. **3**, 013122 (2021).
57. W. W. Zhu, X. S. Fang, D. T. Li, Y. Sun, Y. Li, Y. Jing, and H. Chen, "Simultaneous observation of a topological edge state and exceptional point in an open and non-Hermitian acoustic system," Phys. Rev. Lett. **121**, 124501 (2018).

58. Z. W. Guo, T. Z. Zhang, J. Song, H. T. Jiang, and H. Chen, "Sensitivity of topological edge states in a non-Hermitian dimer chain," Photon. Res. **9**, 574–582 (2021).
59. L. Zhang, Y. H. Yang, Z. Jiang, Q. L. Chen, Q. H. Yan, Z. Y. Wu, B. L. Zhang, J. T. Huangfu, and H. S. Chen, "Demonstration of topological wireless power transfer," Sci. Bull. **66**, 974–980 (2021).
60. J. Song, F. Q. Yang, Z. W. Guo, X. Wu, K. J. Zhu, J. Jiang, Y. Sun, Y. H. Li, H. T. Jiang, and H. Chen, "Wireless power transfer via topological modes in Dimer chains," Phys. Rev. Appl. **15**, 014009 (2021).
61. C. Schmidt, A. Palatnik, M. Sudzius, S. Meister, and K. Leo, "Coupled topological interface states," Phys. Rev. B **103**, 085412 (2021).
62. Y. Jin and K. Yu, "Broadband single-channel coherent perfect absorption with a perfect magnetic mirror," Opt. Express **28**, 35108–35117 (2020).
63. C. Zeng, Y. Sun, G. Li, Y. H. Li, H. T. Jiang, Y. P. Yang, and H. Chen, "Enhanced sensitivity at high-order exceptional points in a passive wireless sensing system," Opt. Express **27**, 27562–27572. (2019).
64. Q. Wang, M. Xiao, H. Liu, S. Zhu, and C. T. Chan, "Optical interface states protected by synthetic Weyl points," Phys. Rev. X **7**, 031032 (2017).
65. G. Du, H. Jiang, Z. Wang, Y. Yang, Z. Wang, H. Lin, and H. Chen, "Heterostructure-based optical absorbers," J. Opt. Soc. Am. B **27**, 1757–1762 (2010).
66. X. Wang, X. Jiang, Q. You, J. Guo, X. Dai, and Y. Xiang, "Tunable and multichannel terahertz perfect absorber due to Tamm surface plasmons with graphene," Photon. Res. **5**, 536–542 (2017).
67. Y. M. Qing, H. F. Ma, and T. J. Cui, "Flexible control of light trapping and localization in a hybrid Tamm plasmonic system," Opt. Lett. **44**, 3302–3305 (2019).
68. G. Lu, F. Wu, M. Zheng, C. Chen, X. Zhou, C. Diao, F. Liu, G. Du, C. Xue, H. Jiang, and H. Chen, "Perfect optical absorbers in a wide range of incidence by photonic heterostructures containing layered hyperbolic metamaterials," Opt. Express **27**, 5326–5336. (2019).
69. H. A. Haus, *Waves and Fields in Optoelectronics* (Prentice-Hall, 1984).
70. S. H. Fan, W. Suh, and J. D. Joannopoulos, "Temporal coupled-mode theory for the Fano resonance in optical resonators," J. Opt. Soc. Am. A **20**, 569–572 (2003).
71. A. Mostafazadeh, "Pseudo-Hermiticity versus PT symmetry: the necessary condition for the reality of the spectrum of a non-Hermitian Hamiltonian," J. Math. Phys. **43**, 205–214 (2002).
72. H. Zhao and L. Feng, "Parity-time symmetric photonics," Nat. Sci. Rev. **5**, 183–199 (2018).
73. J. Yu, B. Ma, A. Ouyang, P. Ghosh, H. Luo, A. Pattanayak, S. Kaur, M. Qiu, P. Belov, and Q. Li, "Dielectric super-absorbing metasurfaces via PT symmetry breaking," Optica **8**, 1290–1295 (2021).